J. Fluid Mech. (2000), *vol.* 418, *pp.* 313–338. Printed in the United Kingdom

Convectively driven exchange flow in a stratified sill-enclosed basin

By T. D. FINNIGAN† AND G. N. IVEY

Centre for Water Research, University of Western Australia,
Nedlands, Perth, Western Australia 6907

(Received 4 June 1999 and in revised form 4 April 2000)

Laboratory experiments are used to investigate the processes governing steady convectively driven circulation in a basin that communicates with a large external reservoir over a shallow sill. The motion is maintained by a steady loss of buoyancy distributed over the surface of the basin. Turbulent convection associated with the forcing produces a horizontal buoyancy gradient across the sill and the resulting mean flow consists of a layer directed into the basin near the surface with a dense counterflow below.

To first order, the magnitude of the exchange flow over the sill is determined by the horizontal momentum balance within the basin. Measurements of the mean and turbulent flow fields are used to show that inertia, buoyancy and friction may each contribute significantly to the balance. The interior flow produces a horizontal pressure gradient near the surface which must also contribute to the momentum balance. The density of the lower layer at the sill reflects the cumulative effect of interior processes, such as mixing, and these in turn influence the hydraulically controlled exchange flow over the sill. The basin dynamics are therefore coupled in a nonlinear fashion with the submaximal sill exchange. This coupling is investigated first by showing how interior processes are affected by changes in the magnitude of the forcing, and then by observing the associated variation of the flow state at the sill. The flow state is defined in terms of its relative proximity to the theoretical maximal exchange limit. Results show that the exchange flows are submaximal with flow rate approximately 85% of the maximal limit. This state appears to change very little in response to increasing forcing.

For a stratified basin, which exhibits a deep stagnant layer under the convectively driven near-surface exchange flow, the possibility of basin ventilation or erosion of deep fluid exists in the long term. This process and its dependence on external parameters is also explored.

1. Introduction

Physical processes in marginal seas and other semi-enclosed natural water bodies have significant effects on both local and far-field environments (e.g. Nihoul 1982). A horizontal buoyancy gradient, caused by localized atmospheric forcing or riverine inflow, can drive circulation within the enclosure and maintain an exchange of fluid with adjoining reservoirs. We consider the specific case of a basin (or sea), partially separated from a large reservoir (or ocean) by a shallow sill, and forced by a steady

† Present address: Department of Oceanography, University of Hawaii at Manoa, HI 96813, USA.

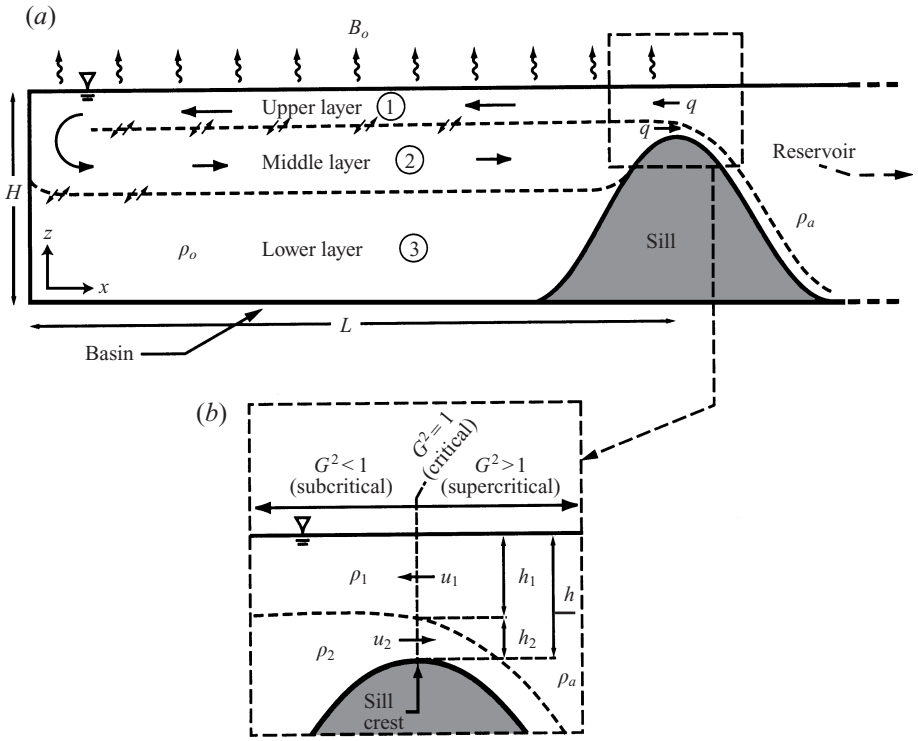

FIGURE 1. Definition sketch for convectively driven flow in a sill-enclosed basin. (*a*) In the basin a mean exchange flow (layers 1 and 2) is driven by the buoyancy flux B_o at the surface while there is a deep stagnant layer (layer 3) below. Mixing regions are indicated by small opposing arrows. The reservoir is assumed to extend indefinitely to the right. (*b*) Close-up view of the sill crest region where the exchange flow is internally hydraulically controlled. The criticality is specified by the value of the composite Froude number G^2, defined in equation (1.1).

loss of buoyancy due to cooling and/or evaporation through the surface (see figure 1*a*). The limited horizontal extent of the forcing results in a buoyancy gradient across the sill and an associated circulation. Fluid enters the basin near the surface, loses buoyancy due to the flux through the surface and then descends near the closed end of the basin. As depicted in figure 1, the finite volume of the enclosure requires a compensatory stream of heavy fluid to exit the basin below the inflow. As an initial condition in our experiments, we include a deep layer of stagnant water which is trapped behind the sill inside the basin. Two prominent and frequently studied examples of this configuration are the Red and Mediterranean Seas. For such systems the topographic control on the flow due to the presence of the constriction plays an important role in the overall dynamics and has been the topic of several studies (see, for example, Armi & Farmer 1988; Garrett, Bormans & Thompson 1990; Bray, Ochoa & Kinder 1995; Murray & Johns 1997; Smeed 1997). The coupling of the flow at the constriction to the forced basin dynamics has been discussed by previous authors (Stommel & Farmer 1953; Maxworthy 1997; Tragou & Garrett 1997; Finnigan & Ivey 1999) but the details of this process are still not completely resolved.

For the present study, laboratory experiments have been conducted in an idealized system as shown in figure 1(*a*) with the intention of determining the processes which govern the steady basin circulation and exchange flow over the sill. While the volume flux q and the density of the outflow at the sill are of interest, as we will show

below, these parameters are not easily specified, being dependent on conditions both in the basin and at the sill itself. In §§ 1.1–1.3 below, we introduce and review internal hydraulic theory, submaximal exchange flows, and previous analytical models of convectively driven basin circulation, all of which are relevant to the present study. Following this, in § 1.4 we introduce the experiments using flow visualization and outline the remainder of the paper.

1.1. *Internal hydraulic control*

Figure 1(*a*) shows how a steady, uniformly distributed loss of buoyancy from the surface of the basin drives an inflow with volume flux q near the surface which, in turn, requires a deeper outflow with equal volume flux. We delineate vertical layers by the sign (+/−) of the mean horizontal velocity component (u). The common surface, or interface, between layers therefore occurs where $u = 0$. The destabilizing surface buoyancy flux produces convective turbulence in the upper layer (layer 1). As will be shown below, the turbulence decays in the middle layer (layer 2) where the fluid is no longer in contact with the forcing surface. Vertical mixing, defined here as the transfer of mass across the interface between layers, may occur within the basin. Near the sill we shall assume that mixing is negligible and that the sill exchange is composed of two distinct layers.

Internal hydraulic theory provides a useful model for this two-layer flow over a sill since it represents a closed-form solution to the inherently nonlinear problem. The theory suggests that the flow is limited, or controlled, at the minimum depth of the sill (the crest) where the phase speed of long internal waves equals the internal convective velocity $u_I \approx (u_1 h_2 + u_2 h_1)/h$, and the composite Froude number (Armi 1986 and references therein)

$$G^2 = \frac{u_1^2}{g' h_1} + \frac{u_2^2}{g' h_2} = 1, \tag{1.1}$$

which is a unique condition termed *critical* flow. This condition relates the local layer velocities u_n ($n = 1, 2$), thicknesses h_n, and densities ρ_n at the sill crest, where $g' = g(\rho_2 - \rho_1)/\rho_2$. In the derivation of (1.1) it is assumed the flow is inviscid, pressure is hydrostatic, velocities are purely horizontal and $g'/g \ll 1$. Although these assumptions are approximately satisfied in our experiments, we are not concerned with the absolute accuracy of (1.1) but rather its ability to represent the essential nonlinear dynamics of exchange at the sill. As discussed by Armi & Farmer (1987), hydraulic theory and the concept of submaximal exchange (described below) are generally applicable even when the assumptions are not strictly met.

For the present experimental configuration the flow is internally supercritical ($G^2 > 1$) outside the basin and internally subcritical ($G^2 < 1$) inside the basin (figure 1*b*). The subcritical basin flow communicates via long internal waves with the hydraulic control at the sill crest. The supercritical section, however, isolates the external reservoir from the basin and sill flows since internal waves do not propagate upstream through it.

Recognizing that $q = u_1 h_1 = u_2 h_2$ at the sill, we rearrange (1.1) and express the volume flux in each layer as

$$q = \left[g' \left(\frac{1}{h_1^3} + \frac{1}{(h - h_1)^3} \right)^{-1} \right]^{1/2}, \tag{1.2}$$

where $h = h_1 + h_2$ is the minimum fluid depth at the sill. Conservation of buoyancy

for the control volume of the basin at steady state further requires

$$qg' = B_o L, \tag{1.3}$$

and therefore

$$q = \left[B_o L \left(\frac{1}{h_1^3} + \frac{1}{(h - h_1)^3} \right)^{-1} \right]^{1/3}, \tag{1.4}$$

where B_o is the surface buoyancy flux and L is the length of the forced basin. Equation (1.3) states that, when the flow is steady, the buoyancy transported across the sill is identical to the amount lost through the surface inside the basin. It follows from (1.4) that the volume flux q, and therefore also g', is known if the depth of the upper layer at the sill is known. However, h_1 is generally not known and is dependent on conditions within the basin. Because of this, (1.4) is not a closed-form solution for q in terms of external fixed parameters.

It is of interest to know how the processes within the basin influence the exchange flow at the sill. The following questions naturally arise. What are the significant terms in the momentum balance within the basin? How are interior conditions and the sill exchange coupled and, therefore, how do h_1 and q depend on B_o? Does interior mixing influence the exchange and if so, what mechanism is responsible for this mixing and how does it depend on external parameters?

In this paper we attempt to answer these questions using experimental observations. To interpret our results concerning the controlled exchange we use the concept of submaximal exchange, which is now reviewed in the context of our experimental configuration.

1.2. *Submaximal exchange flow*

Stommel & Farmer (1953) recognized the ability of a constriction to control the flow into and out of an estuary. They demonstrated the dependence of the exchange on the density difference between layers at the constriction, and therefore, on mixing conditions within the basin. In addition, Stommel & Farmer (1953) suggested that, for a particular value of the density difference, or g', there must exist a maximum possible exchange rate. This special limit is commonly referred to as *maximal exchange* and it is often associated with the so-called *overmixed* state of an estuary (e.g. Farmer & Armi 1986; Garrett *et al.* 1990). Where the constriction is represented simply as a sill (as in the present paper), Farmer & Armi (1986) indicated a range of possible *submaximal* exchange flows. Within this range the thickness of the upper layer at the sill crest h_1 was shown to be in the range $0.625h < h_1 < h$. The maximal volumetric exchange occurs at the lower bound ($h_1 = 0.625h$) of this range, and from (1.4) it is given by

$$q_{me} = 0.35(B_o L)^{1/3} h, \tag{1.5}$$

which is a theoretical prediction for the exchange rate between two basins, each having an infinitely thick lower layer away from the sill region. In the experiments described here the lower layer has finite thickness. In practice, this will produce slightly higher exchange rates than predicted by the theory (Farmer & Armi 1986). Nevertheless, we shall retain (1.5) and use it as a conservative estimate of the maximal exchange limit for the experiments.

The proximity of the exchange to the maximal limit is determined by interior processes. It is therefore convenient to refer to the exchange *relative* to the maximal limit (for which h_1 is known) rather than the absolute exchange q. We define the

relative volumetric exchange

$$q_* = \frac{q}{q_{me}} = \left[0.35h\left(\frac{1}{h_1^3} + \frac{1}{(h-h_1)^3}\right)^{1/3}\right]^{-1}, \tag{1.6}$$

which indicates the location of the flow state within the submaximal range $0 < q_* < 1$, where the upper bound is the maximal exchange limit. Although the forcing parameter B_o does not appear as an independent variable in (1.6) its effect is implicitly included in the variable h_1.

Finnigan & Ivey (1999) reported experiments in a basin similar to the one considered here (except without a stagnant lower layer) and noted that the inflow velocity is determined by the magnitude of B_o and the geometric scales of the system. Assuming initially an inertia–buoyancy balance within the basin they showed how internal processes, including friction, may be accounted for when the balance is applied at the sill and coupled with the hydraulic control condition (1.1). Using experimental results, Finnigan & Ivey (1999) demonstrated that a change in B_o results in a change in h_1 (and therefore q_*) and a shift to a new equilibrium state between the flow at the sill and the basin interior conditions. In general q_* was found to decrease with increasing B_o and, although they noted that mixing processes influence the shift, they did not provide detailed observations from within the basin.

1.3. *Previous analytical models*

The observed circulation of the Red Sea has initiated a few attempts to develop a reasonably simple analytical model to describe the flow. While our study is not necessarily concerned with the Red Sea, the configuration is similar in both cases, and since these previous studies have explored possible momentum balances and mixing situations, with and without hydraulic control, they are worth reviewing here in brief.

Phillips (1966) considered the circulation in an idealized basin similar to that shown in figure 1 and derived similarity solutions for two-dimensional flow in a vertical plane. The formulation was analogous to that for a turbulent boundary layer and thus represented a three-way inertia–buoyancy–viscous balance in the horizontal direction. The fluid buoyancy was defined as

$$b = -g\left(\frac{\rho - \rho_o}{\rho_o}\right), \tag{1.7}$$

where ρ_o is a constant reference density, typically taken as the density of fluid in the deep stagnant layer. We shall adopt the same definition and refer to fluid buoyancy rather than density for the remainder of the paper. In Phillips (1966), equations for mean horizontal velocity u and buoyancy b were expressed as

$$u(x,z) = f(z/h)(B_o x)^{1/3}, \quad b(x,z) = g(z/h)\frac{(B_o x)^{2/3}}{h}, \tag{1.8}$$

where $f(z/h)$ and $g(z/h)$ are non-dimensional vertical shape functions. For the internal turbulent stress, or Reynolds stress, to balance the inertia and buoyancy terms in the momentum equation,

$$\overline{u'w'}(x,z) = h(z/h)\frac{B_o^{2/3}h}{x^{1/3}}, \tag{1.9}$$

where $h(z/h)$ is another shape function. Vertical buoyancy profiles recorded (by previous researchers) at several locations along the Red Sea appeared to scale in

accordance with the theory, thus providing an indication of the form of $g(z/h)$. Since the shape functions f, g and h are generally unknown, detailed comparisons with field data were not possible.

Tragou & Garrett (1997) showed that a simple steady-state balance between the longitudinal buoyancy gradient and inertia forces in the upper layer of the Red Sea predicts a much larger mean flow speed than that observed. They thus concluded that friction is of first-order importance in the momentum balance and, using the same theory as Phillips (1966), they suggested a parameterization of the turbulent momentum flux and buoyancy flux fields, allowing them to solve the analytical system. They then extended the solutions to include such factors as sidewall drag and non-uniform channel cross-section. By comparing results with observations from the Red Sea, they showed how these external factors could influence the circulation. Although the theory does not explicitly account for the presence of a sill, the probable effects of one were discussed in context with the concept of maximal/submaximal exchange.

Maxworthy (1997) pointed out that it is essential to include the effects of an internal hydraulic control at the entrance to the sea – a feature which is not accounted for in the theory of Phillips (1966). This was included in a model developed by Maxworthy (1997) which was based on a two-component force balance between buoyancy and friction and an assumption of zero vertical mixing within the basin. The model assumptions led to equations similar in form to (1.8) except with coefficient functions (f, g and h) varying horizontally rather than vertically in each layer. The same buoyancy data used to compare with the buoyancy scaling of the Phillips (1966) model were shown also to be consistent with the scaling of Maxworthy's (1997) model despite the neglect of mixing. Significant mixing was actually observed in the Red Sea data and Maxworthy (1997) suggested that the Richardson number was too great everywhere along the length of the sea to expect local shear instabilities as a possible mechanism for driving local vertical mixing. The detailed investigation of processes which could be responsible for vertical mixing is one of the main goals of the present study.

In summary, while there are fundamental differences in previous modelling approaches, it is generally agreed that a hydraulic control at the entrance and significant friction within the sea both play an important role in the dynamics. It is also clear that mixing affects the buoyancy of the outflowing layer and hence the control of the flow at the sill.

1.4. *The present experiments*

The experiments reported herein are intended to simulate the buoyancy-driven submaximal exchange in a general sill–basin system which is frictionally influenced, hydraulically controlled at the sill, and exhibits some vertical mixing within the basin. The experimental methods used are described in the following section. The horizontal momentum balance which establishes the magnitude of the circulation in the basin is described in § 3 where detailed measurements of the turbulence field allow us to suggest a source of internal friction capable of balancing the effects of inertia and buoyancy. In § 4 we investigate the process and effect (on the sill exchange) of vertical mixing within the basin. This leads to a description of the inter-dependence between the submaximal exchange at the sill and mixing within the basin, which combines with the momentum balance in determining the overall equilibrium steady state of the system.

An additional feature of the flows described here is the ability of the circulating layers to slowly erode the deep stagnant fluid in layer 3. Turbulence energy, produced

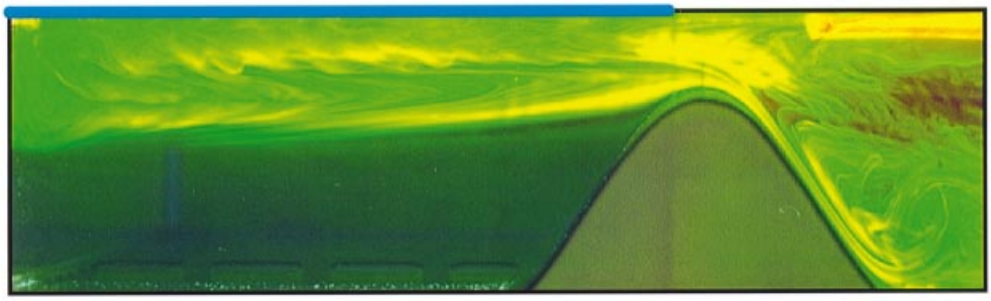

(*a*) Experiment 6

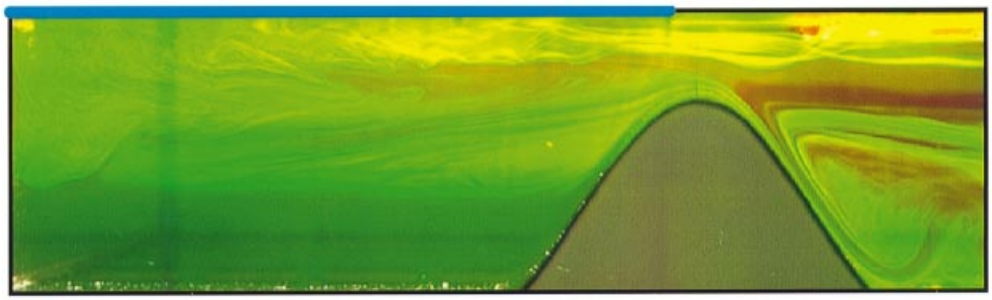

(*b*) Experiment 7

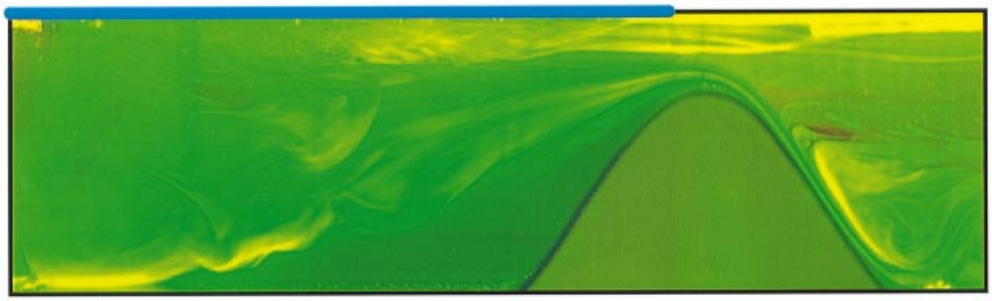

(*c*) Experiment 8

FIGURE 2. Photographs of three visualization experiments each subjected to a progressively larger surface buoyancy flux B_o (applied over the surface region marked in blue). Each photograph was taken at approximately the same time relative to the start of the experiment. The parameters for each experiment are given in table 1.

by convective forcing at the surface, is advected downwards at the end of the basin by the mean flow (see figure 1). This energy is available for entrainment of heavy fluid from layer 3 into layer 2, but the process diminishes with horizontal distance from the head of the basin as the turbulence intensity decays. In figure 2 we present photographs of three visualization experiments which will be discussed further in § 5 below. Each experiment had a similar initial stratification but was forced with a different value of B_o. The elapsed time since the beginning of the experiment is approximately the same in each case. Some features worth noting at this stage are:

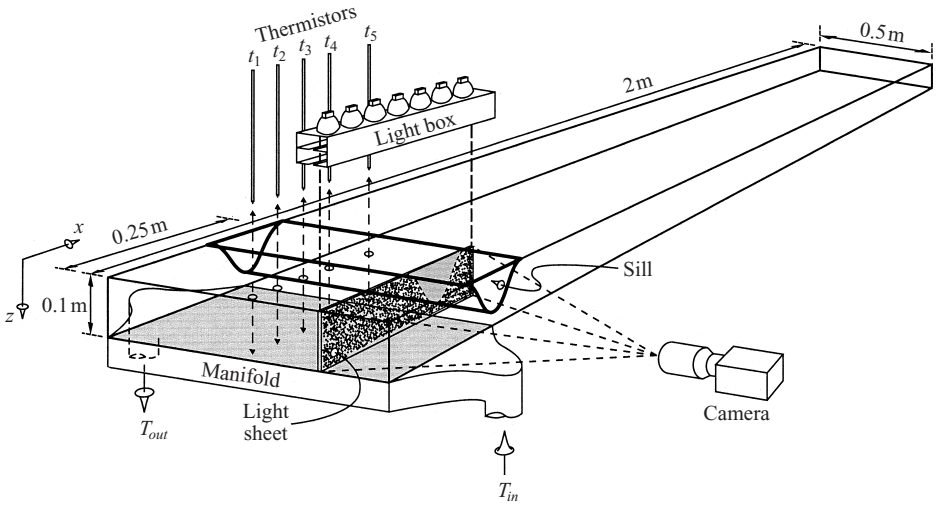

FIGURE 3. Sketch of the experimental apparatus. For convenience the sill was attached to the upper surface of the tank with the buoyancy flux applied over the bottom (shaded) surface within the basin. All subsequent results are presented in the inverted, geophysically relevant, orientation.

evidence of hydraulic control at the sill (horizontal asymmetry at the crest and a plunging outflow down the outside of the sill), convective turbulence in layer 1, and erosion of the deep stagnant layer which is significantly enhanced with increasing B_o. The erosion process is described in § 5 and the paper concludes with a general discussion of the observations, their interpretation, and implications for other basins (§ 6).

2. Experimental methods

2.1. *Apparatus*

The laboratory experiments were performed in an insulated rectangular tank 2 m long, 0.5 m wide and 0.1 m deep using fresh water as the working fluid. The same facility was previously described by both Sturman & Ivey (1998) and Finnigan & Ivey (1999) who reported related experimental studies. For the present work, the sill was located 0.26 m from one end of the tank and an outward buoyancy flux condition was applied over the surface of the resulting basin (figure 3). The forced area covered the width of the basin and extended 0.25 m from the endwall. For practical reasons the experiments were performed 'upside-down' with the sill attached to the upper surface and buoyancy forcing at the lower surface. Flows produced in this orientation are exact inversions of those for the natural orientation except that buoyancy, as given by (1.7), must be multiplied by -1. The vertical orientation is therefore irrelevant and we shall present all further discussion and results in the usual orientation (as shown in figure 1).

A thermally generated buoyancy flux was established by circulating heated water through a manifold behind a copper plate acting as the basin surface. The temperature difference $\Delta T = |T_{tank} - T_{manifold}|$ between the tank and manifold fluids resulted in a buoyancy flux through the copper plate. In general, ΔT varied in the range 5–20°C while the spatial variation of temperature along the inside surface was $O(0.1\Delta T)$. The heat flux through the copper plate was therefore nearly spatially uniform in all cases.

Experiment	$B_o \times 10^6$ ($m^2\,s^{-3}$)	Purpose	$q \times 10^4$ ($m^2\,s^{-1}$)	g' ($m\,s^{-2}$)
1	0.4	Q	0.39	0.0036
2	0.9	Q	0.56	0.0029
3	3.0	Q	0.82	0.0068
4	6.0	Q	1.02	0.0080
5	0.4	V	—	—
6	0.9	V	—	—
7	3.0	V	—	—
8	6.0	V	—	—

TABLE 1. List of experiments performed for both quantitative analysis (Q) and for flow visualization (V). Volume flux q and reduced gravity g' were measured at the sill crest. These measurements are discussed in §4.2.

Temperature was monitored at the manifold inlet T_{in} and outlet T_{out} along with the flow rate Q through the manifold so that the average heat flux through the plate could be determined as

$$H = \rho C_p |T_{in} - T_{out}| Q, \tag{2.1}$$

and therefore the average buoyancy flux as

$$B_o = \frac{\alpha g H}{\rho C_p A}, \tag{2.2}$$

where A is the surface area of the plate, and the coefficient of thermal expansion α, the specific heat C_p and the density ρ were determined at the average manifold fluid temperature. Accounting for spatial variations and measurement resolution, we estimate the reported B_o values to be accurate within $\pm 10\%$.

2.2. *Initial conditions and unsteady flow*

Before each experiment the tank was filled with fresh water at the laboratory temperature. To establish the initial stratification within the basin a relatively large surface buoyancy flux B_s was applied until turbulent convection had mixed the basin and a steady exchange with the external reservoir was established. The buoyancy flux was then switched off and the system allowed to come to rest leaving ambient reservoir fluid ($b = b_a$) above the sill level in the basin and relatively dense fluid ($b < b_a$) trapped behind the sill.

An experiment was begun by applying a surface buoyancy flux B_o with magnitude $\leqslant B_s$. The values of B_o used for each experiment are listed in table 1. Experiments 1–4 were intended primarily for data acquisition and experiments 5–8 for flow visualization.

Initiation of the forcing was followed by the diffusive growth of a thermal boundary layer adjacent to the forcing surface. Soon after, instability of the boundary layer led to turbulent convection which rapidly penetrated the region of ambient fluid above the height of the sill crest. As described in detail previously by Finnigan & Ivey (1999), the buoyancy gradient established between this convecting fluid and the external reservoir fluid outside the basin resulted in the initiation of an exchange flow at the sill and the subsequent propagation of a velocity front across the basin. The flow became approximately steady after the front reached the endwall of the basin ($x = 0$). In this paper we are only concerned with the dynamics after this stage

has been reached. For our analysis we consider the upper layers (1 and 2) of the circulation to be steady although it may be more appropriate to refer to the flow as quasi-steady due to the possibility of slow erosion of the deep stagnant layer below (see figure 2 and § 5).

2.3. *Measurements*

2.3.1. *Buoyancy*

Measurements of temperature were made in order to determine the mean buoyancy field $b(x, z)$. A horizontal array of fast-response thermistors (labelled t_1–t_5 in the x-direction in figure 3) was used periodically to sample the temperature of the fluid in the basin and at the sill. The thermistors traversed the depth of the basin at regular 60 s intervals while sampling at 100 Hz, yielding spatial resolution of the temperature field to 1 mm with accuracy $\pm 0.003^{\circ}$C. Temperature recordings were converted to density units using a high-order empirical equation of state and buoyancy was then calculated from (1.7).

2.3.2. *Velocity*

Velocity measurements were made in order to resolve both the mean and turbulent flow fields. Measurements within a vertical (x, z)-plane oriented along the basin were obtained using the digital particle tracking velocimetry (DPTV) technique developed and described by Cowen & Monismith (1997). The method is similar to standard particle image velocimetry (PIV) in that it derives an instantaneous two-dimensional velocity field from a pair of images taken a short time duration apart. PIV techniques typically use statistical methods to determine displacements (between two images) of small patterns in a particle seeded flow (e.g. Raffel, Willert & Kompenhans 1998). The DPTV technique employed here relies on a course-resolution PIV algorithm to reveal the large-scale velocity field. This field is then used by the DPTV routine as a guide in the identification and tracking of individual particles. The latter process produces a vector field with significantly finer spatial resolution and with subpixel spatial accuracy.

For the present experiments the fluid was seeded with pliolite particles which were illuminated by a light sheet projected through the upper surface of the tank. The light sheet was produced by a simple linear arrangement of halogen lamps which were focused by a series of narrow slits (see figure 3). A 1024×1024 pixel resolution digital camera oriented at 90° to the light sheet captured pairs of particle images at regular 3.9 s intervals with an inter-image delay of 0.12 s. A total of 506 image pairs, transferred direct from camera to computer disk, were accumulated during each experiment.

From the description of the method given by Cowen & Monismith (1997) we expect the DPTV technique to resolve velocity structure to approximately 2 mm using our image resolution (3.5 pixels mm^{-1}) and inter-image delay. Close to the forcing surface where convective turbulence is present (see § 3.2), we expect the rate of dissipation ϵ of turbulent kinetic energy (TKE) to scale with the surface buoyancy flux B_o (e.g. Shay & Gregg 1986). Mean values of ϵ/B_o obtained from field measurements lie in the range 0.44–0.87 (Anis & Moum 1994) and we therefore estimate the Kolmogorov length scale in the experiments as

$$\eta \sim \left(\frac{\nu^3}{\epsilon}\right)^{1/4} \sim \left(\frac{\nu^3}{0.6B_o}\right)^{1/4}, \tag{2.3}$$

where ν is kinematic viscosity. For experiment 4, which has the largest B_o, $\eta \sim 1$ mm.

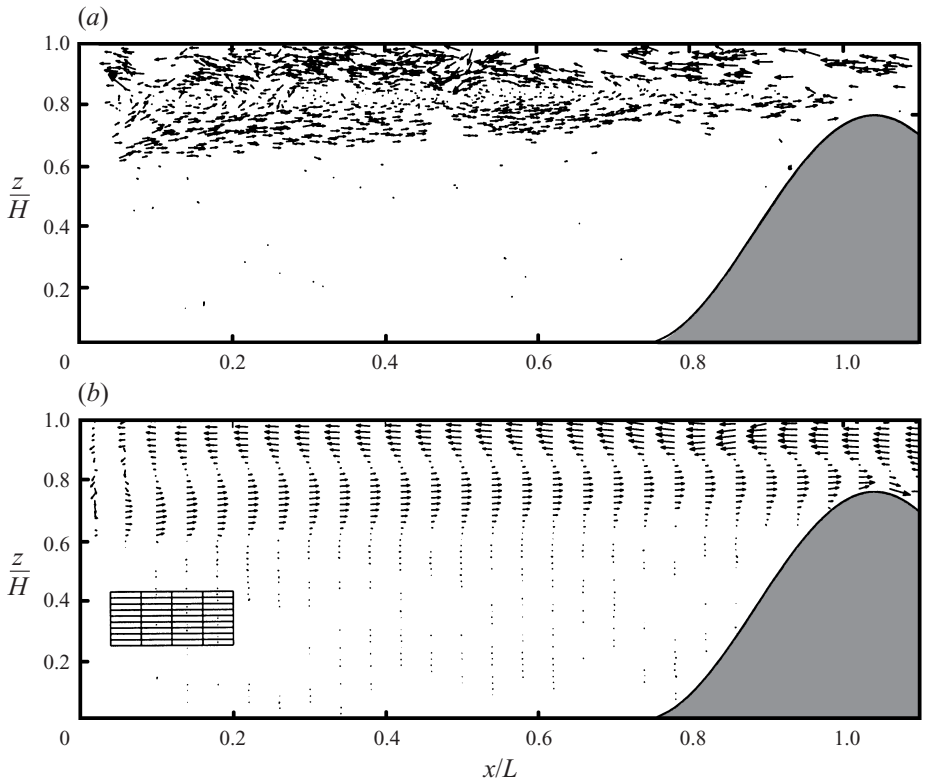

FIGURE 4. (*a*) A raw instantaneous DPTV vector field from experiment 1. (*b*) The mean velocity field obtained by averaging the binned velocity data over the duration of the experiment (while at steady state). A small portion of the domain has been segmented to illustrate the bin arrangement used throughout the domain.

These scales are therefore nearly resolved by the DPTV method in theory. However, imperfect particle seeding density, particle distribution and lighting conditions do affect the measurements and we estimate that our system is capable of resolving structures of $\approx 4\eta$. Since 99% of the dissipation spectrum takes place for wavenumbers $k < 5.5\eta^{-1}$, the smallest scales need not be resolved in order to fully characterize the flow (Cowen & Monismith 1997).

In each velocity field individual vectors are located at the average (between the two images) position of the tracked particle. An example of one such field (taken from experiment 1) which contains approximately 1100 tracked particles (vectors) is shown in figure 4(*a*). In order to obtain the mean and turbulent fields the flow domain was first segmented into rectangular bins, each 10 mm wide by 2 mm high. This resulted in 51 bins in the vertical direction and 28 bins in the horizontal. Data from up to 350 individual velocity fields per experiment (all acquired after the flow had reached steady state) were sorted into the bins. Each bin then contained $O(800)$ vectors and the total number of accumulated vectors in the flow domain during an experiment was $O(5 \times 10^5)$.

The mean velocity at each bin location was computed as the ensemble average over all the vectors located within the bin. The resulting mean velocity field for experiment 1 is shown in figure 4(*b*) where the tail of each vector marks the centre of a bin. In a portion of the domain some of the bin boundaries are drawn for reference. Turbulent

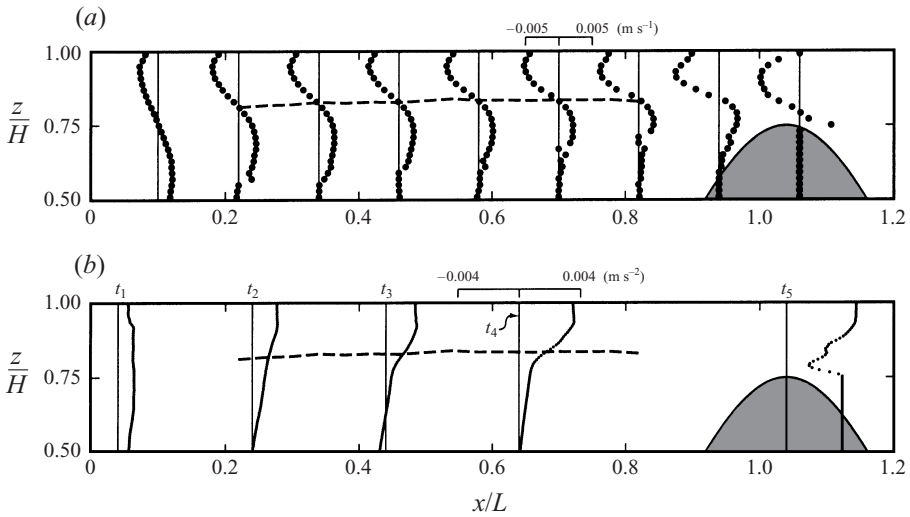

FIGURE 5. Vertical profiles of (*a*) mean horizontal velocity and (*b*) mean buoyancy for experiment 2 over the top half of the basin. Buoyancy profiles, referenced to the constant buoyancy of the bottom layer (ρ_o), were measured along the vertical lines shown in (*b*) which indicate the thermistor locations (labelled t_1–t_5). In both plots the interface between layer 1 and layer 2 is shown as a dashed line.

fluctuating components u' and w' were obtained at each bin location by subtracting the local mean velocity from the individual (total velocity) vectors. From these data various quantities required for the following analysis, such as turbulent (Reynolds) stress and r.m.s. velocity, were computed.

3. Momentum balance

The entire circulation in the basin is driven by the lateral buoyancy gradient within the upper layer. This gradient, established and maintained by the surface buoyancy flux through the process of turbulent convection, is what draws fluid in from the external reservoir. The deeper return flow in layer 2 is a passive response required to conserve volume in the basin. This return layer plays an active role in the exchange at the sill crest where it is directly controlled (see Farmer & Armi 1986). In this section we examine the horizontal and vertical structure of the upper layer. The observations are then used to describe the horizontal momentum balance which dictates the magnitude of the circulation and exchange rate q. The precise value of q is of course dependent on the sill control and the associated equilibrium state which is described in § 4.2.

3.1. *Non-dimensional scaling*

In proceeding to explain the general structure of the upper layer we first wish to note some features common to all of the experiments. Results from experiment 2 are used as an example. Figures 5(*a*) and 5(*b*) show profiles of mean horizontal velocity and mean buoyancy, respectively, where only the upper half of the basin is shown. A dashed line indicates the interface ($u = 0$) between layer 1 and layer 2 within the basin. Note that the magnitude of the velocity and buoyancy profiles varies gradually along the basin (except near the endwall and the sill). The thickness of layer 1 exhibits a small increase with decreasing x suggesting a slight divergence of the flow in the

upper layer as the end region is approached. Similar behaviour was observed in all of the experiments.

These observations suggest the existence of non-dimensional forms of the measured variables, which essentially remove the dependence on B_o and x. Following the scaling of Phillips (1966) and Finnigan & Ivey (1999) (based on an inertia–buoyancy–friction balance) possible non-dimensional forms of mean horizontal velocity, mean buoyancy, and Reynolds stress are

$$u_* = \frac{u}{(B_o x_v)^{1/3}}, \tag{3.1}$$

$$b_* = \frac{bh}{(B_o x_v)^{2/3}}, \tag{3.2}$$

$$\overline{u'w'_*} = \frac{\overline{u'w'}\, x_v^{1/3}}{B_o^{2/3} h}, \tag{3.3}$$

respectively. Note that these quantities may still vary with z. The horizontal coordinate x_v is referred to a *virtual* origin which is defined below. For convenience, horizontal and vertical position within the basin is represented non-dimensionally by

$$x_* = \frac{x_v}{L}, \quad z_* = \frac{z}{H}. \tag{3.4}$$

Although the endwall of the basin ($x = 0$) is a physical boundary it does not represent the origin for which the scaling associated with (3.1)–(3.3) applies. The virtual origin ($x_v = 0$) for the velocity scaling actually lies outside the basin, beyond the endwall (see figure 6*b*). Figure 6(*a*) shows the variation along the basin of the mean horizontal velocity (magnitude) $|u|$ in the upper layer for experiments 1–4. The velocity data were extracted along a horizontal line at about the mid-depth of the upper layer. In the central region of the basin, away from endwall and sill effects, u increases with x and in general, u also increases with B_o. From (3.1) we note that $|u^3/B_o|$ is expected to vary linearly along the basin. This scaling parameter is shown in figure 6(*b*) where the data collapse reasonably well onto a straight line within a section S in the central portion of the basin, in support of the scaling associated with (3.1), and therefore (3.2)–(3.3), which are based on the same assumptions (Phillips 1966; Finnigan & Ivey 1999). The confirmation of this velocity scaling is in general agreement with the results of Sturman & Ivey (1998) where a different basin geometry without a sill was the subject of a similar laboratory experiment. In figure 6(*b*), a least-squares linear fit to the data (solid line) within S locates the virtual origin ($x_v = 0$) at $x/L = -0.22$ or $x = -0.06$ m outside the basin (indicated by the dashed line). This point therefore represents the average virtual origin location for velocity in the four experiments. It does not correspond to the endwall location because that would require the linear horizontal profile to intersect the $x = 0$ origin in figure 6(*b*), which is a non-physical expectation. Similarly, a unique virtual origin location may also be found for buoyancy† and measurements indicate that it lies at $x/L = 0.1$. Analogous methods have been used by Phillips (1966) and Tragou & Garrett (1997) to locate the virtual origin for buoyancy in the Red Sea and indeed they found $x_v = 0$ some 160 km southeast of Suez, which translates to a point with $x > 0$, in agreement with our experimental findings. It is not as easy to locate the virtual origin for Reynolds

† For notational simplicity we refer generally to horizontal distance x_v with respect to the virtual origin. The reader should note that each dynamic variable is actually associated with a unique virtual origin location.

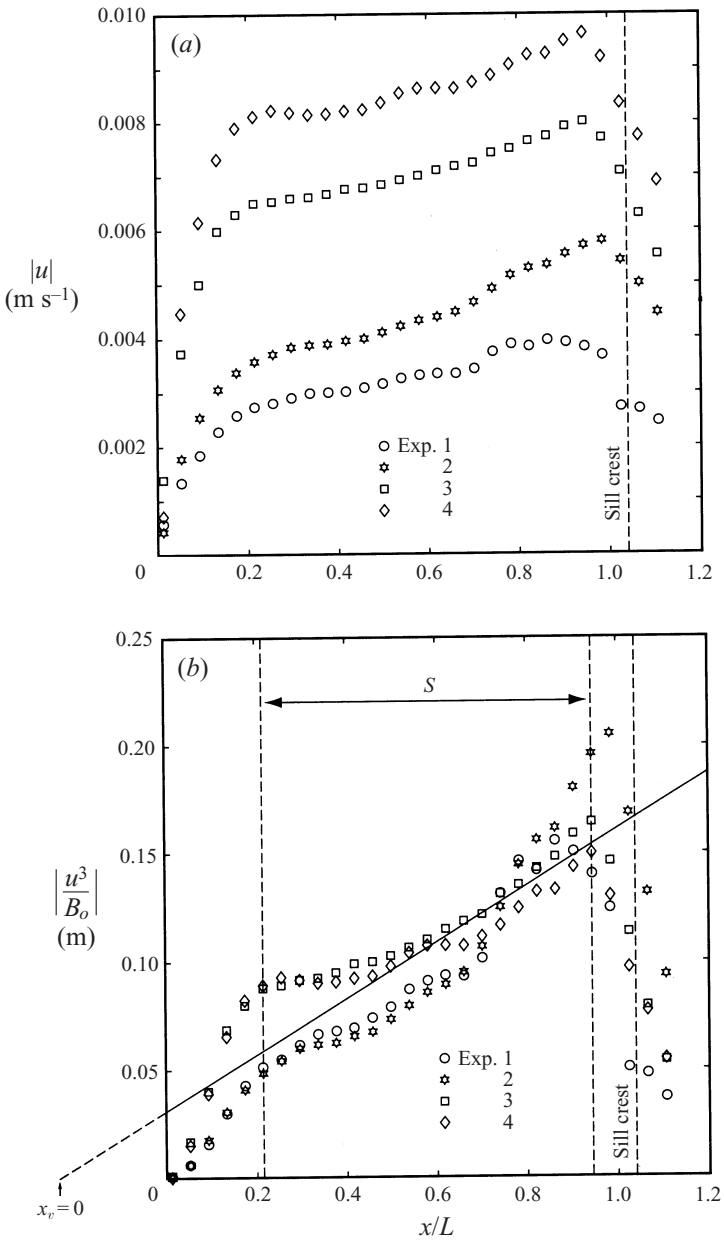

FIGURE 6. (*a*) Along-basin variation of mean upper-layer horizontal velocity. (*b*) Variation of the scaling parameter $\left|u^3/B_o\right|$ along the basin. A solid line, fitted to the data within the interior section *S*, indicates the scaling associated with equation (3.1) and is extended (dashed line) to the *virtual* origin ($x_v = 0$).

stress but we shall assume that it roughly coincides with that for the mean horizontal velocity.

3.2. *Structure of the upper layer*

Scaled profiles of horizontal velocity, buoyancy and Reynolds stress are shown in figures 7(*a*), 7(*b*), and 7(*c*) respectively. Only the portion of the flow *above* the sill

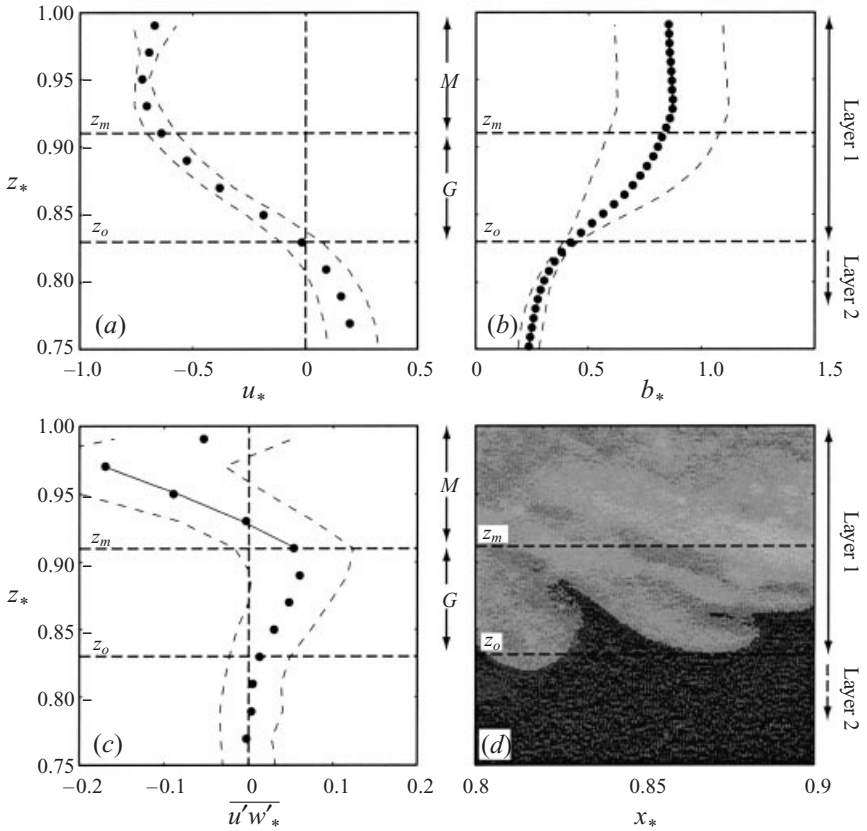

FIGURE 7. Structure of the upper layer shown as profiles of (*a*) non-dimensional mean horizontal velocity u_*, (*b*) non-dimensional mean buoyancy b_*, (*c*) non-dimensional Reynolds stress $\overline{u'w'_*}$, and (*d*) a sample photographic image from experiment 5. Thin dashed lines indicate $\pm\sigma$. Note that only the top quarter of the basin depth is shown here so that the structure of the upper layer may be seen clearly. See text for further details.

crest ($z_* \geqslant 0.75$) is shown so that details of the upper layer may be seen clearly. Each of the profiles shown (as large dots) represents the ensemble average of several individual measured profiles obtained within section *S*. For example, there are 15 horizontal velocity bins within *S*. A single dimensional profile may be obtained from each horizontal bin location. For each of experiments 1–4 there were 350 individual velocity fields acquired at steady state so that

$$4 \text{ experiments} \times \frac{350 \text{ fields}}{\text{experiment}} \times \frac{15 \text{ profiles}}{\text{field}} = 21 \times 10^3 \text{ dimensional profiles}, \quad (3.5)$$

contributed to the velocity profile shown in figure 7(*a*). The same number make up the Reynolds stress profile (figure 7*c*) while the buoyancy profile resulted from 384 dimensional profiles. The thin dashed lines in figure 7 indicate $\pm\sigma$, one standard deviation about the mean profile. The fact that the data collapse reasonably well onto single profiles for each of u_*, b_* and $\overline{u'w'_*}$ lends further support for the scaling proposed in (3.1)–(3.3). The profiles introduced here represent data ranging over values of B_o and x_v and, as described in the next subsection, they may be used to evaluate terms in the basin-scale momentum balance.

A vertical dashed line at $u_* = 0$ in figure 7(a) delineates the ensemble average of the position of the interface between the upper layer ($u_* < 0$) and the middle layer ($u_* > 0$). The temporally averaged interface position actually varies slightly with x_v and B_o (see figure 5). The intersecting horizontal dashed line at $z_* \approx 0.83$ indicates the level of the ensemble-averaged interface position, which we denote by z_o. This level is also indicated in figures 7(b), 7(c), and 7(d), the last of which is a photographic segment from the interior portion of experiment 5, where the fluid in the upper layer has been dyed.

Looking at all four panels in figure 7, it is clear that within the upper layer there are two distinct regions: (i) a mixed region (M) adjacent to the surface ($z_m < z_* < 1$) and (ii) a gradient region (G) adjacent to the $u_* = 0$ interface ($z_o < z_* < z_m$). Referring specifically to figure 7(d) we note that the gradient region consists of fluid from both the upper and middle layers. From 7(c) it is apparent that turbulent stress decreases with depth towards z_o and is, on average, negligible for $z_* < z_o$ (middle layer). It thus appears that convective turbulence in the upper layer drives entrainment from the middle layer into the mixed region of the upper layer with the gradient region acting as a conduit. The details of this process, its similarity to previous one-dimensional experiments, and its implications for the overall exchange flow are discussed in § 4.

3.3. *Evaluation of the momentum balance*

Along the upper layer in the basin we assume a *mixed layer* or *slab* model, reminiscent of the one-dimensional models of, for example, Niiler & Kraus (1977) and Tennekes & Driedonks (1981), except in this case we allow horizontal variations. Such models rely on the existence of a well-mixed region (or slab) below the surface. Within this region u and b do not vary vertically although $\overline{u'w'}$ may. Referring to figure 7, we recognize such a mixed region (M) within which we shall apply the model and assess the momentum balance.

Conservation of horizontal momentum in the mixed region M may be expressed, in dimensional variables, as

$$u\frac{\partial u}{\partial x} = -\frac{1}{\rho_o}\frac{\partial P}{\partial x} - \frac{\partial \overline{u'w'}}{\partial z}, \tag{3.6}$$

where the effects of molecular viscosity are assumed negligible and P is the deviation of the pressure from hydrostatic conditions in a fluid of uniform density ρ_o. In the vertical direction the momentum equation has the form

$$\frac{1}{\rho_o}\frac{\partial P}{\partial z} = b - \frac{\partial \overline{w'w'}}{\partial z}, \tag{3.7}$$

which we differentiate with respect to x before integrating vertically, from within the mixed region to the surface ($z = H$), leading to

$$\frac{1}{\rho_o}\frac{\partial P}{\partial x} = \frac{\mathrm{d}b}{\mathrm{d}x}z - \frac{\partial \overline{w'w'}}{\partial x} + \frac{1}{\rho_o}\frac{\mathrm{d}P_s}{\mathrm{d}x}, \tag{3.8}$$

where the last term represents the horizontal pressure gradient at the surface. In the laboratory this pressure gradient is supported by the rigid lid at $z = H$, which is analogous to the field case where $\mathrm{d}P_s/\mathrm{d}x = \rho_o g'(\mathrm{d}\eta/\mathrm{d}x)$, due to the slope of the free surface, $\eta(x) = z - H$. By combining (3.8) with (3.6) we obtain

$$u\frac{\mathrm{d}u}{\mathrm{d}x} + \frac{\mathrm{d}b}{\mathrm{d}x}z + \frac{1}{\rho_o}\frac{\mathrm{d}P_s}{\mathrm{d}x} = -\frac{\partial \overline{u'w'}}{\partial z} + \frac{\partial \overline{w'w'}}{\partial x}, \tag{3.9}$$

and, for the boundary layer flow of interest,

$$\frac{\partial \overline{u'w'}}{\partial z} \gg \frac{\partial \overline{w'w'}}{\partial x} \tag{3.10}$$

(Phillips 1966). Inserting the scaled forms (3.1)–(3.3) into the differential equation (3.9) leads to a non-dimensional algebraic equation,

$$\frac{1}{3}u_*^2 + \frac{2}{3}\frac{H}{h}b_*z_* + \frac{1}{\rho_o}\frac{\mathrm{d}P_s}{\mathrm{d}x}\frac{(x_*L)^{1/3}}{B_o^{2/3}} = -\frac{h}{H}\frac{\mathrm{d}\overline{u'w'_*}}{\mathrm{d}z_*}. \tag{3.11}$$

Integrating (3.11) across the mixed region from $z_* = z_m$ to $z_* = 1$ leads to

$$\underbrace{\frac{1}{3}u_*^2(1-z_m)}_{I} + \underbrace{\frac{1}{3}\frac{H}{h}b_*(1-z_m^2)}_{B} + \underbrace{\frac{1}{\rho_o}\frac{\mathrm{d}P_s}{\mathrm{d}x}\frac{(x_*L)^{1/3}}{B_o^{2/3}}(1-z_m)}_{P} = \underbrace{-\frac{h}{H}\Delta\overline{u'w'_*}}_{T}, \tag{3.12}$$

where $\Delta\overline{u'w'_*}$ is the difference in $\overline{u'w'_*}$ across the mixed region. From the profiles shown in figure 7 it is clear that the first two terms in (3.11) are positive. The lateral buoyancy gradient in the upper layer results in a negative pressure gradient in the middle layer which drives the outflow. To conserve volume in the basin a corresponding inflow is required and therefore a positive surface pressure gradient $\mathrm{d}P_s/\mathrm{d}x > 0$ develops. These results indicate that the term on the right-hand side must be positive. Indeed, the measured profile of $\overline{u'w'_*}$ (figure 7*c*) is negative across the mixed layer, which confirms this.

Polarity of the Reynolds stress profile about the $\overline{u'w'_*} = 0$ line indicates a turbulent flux of horizontal momentum directed downwards ($\overline{u'w'_*} > 0$) near the bottom of the mixed region ($z_* \lesssim 0.93$) and upwards ($\overline{u'w'_*} < 0$) at the top of the mixed region ($z_* \gtrsim 0.93$). This occurs because momentum is lost to the counterflowing middle layer below and to the thin viscous boundary layer at the surface (e.g. Tennekes & Driedonks 1980).

Since buoyancy drives the flow we know that B must be an important term in (3.12). To maintain the inflow we also expect term P to factor significantly in the momentum balance. The question is, do the inertia and turbulent stress terms contribute to the balance? Aside from P, terms in (3.12) may be estimated from the data shown in figure 7, which gives $I \sim 0.1$, $B \sim 0.3$, and $T \sim 0.1$. These terms are of similar magnitude consistent with a balance having significant contributions from each of the terms in (3.12). This balance is largely responsible for the magnitude of the volume flux q at the sill. At a more detailed level, the value of q is subject to the constraint imposed by hydraulic control and thus depends on recirculation within the basin, to which we now turn our attention.

4. Recirculation and sill–basin equilibrium

In § 1.2 we described how the vertical transport of fluid across the $u = 0$ internal boundary in the moving upper layers influences the exchange at the sill. The analysis in § 3.2 showed that, in general, fluid is transported from the middle layer into the upper layer. We now examine this transport to determine its dependence on the forcing and basin geometry and its overall effect on the circulation.

4.1. *Entrainment and recirculation*

As noted above in § 3.2, fluid in the upper layer is stirred by convective turbulence, while the middle return layer is essentially laminar. This is evidently due to the

rapid decay of the turbulence in the flow after it departs from the forcing surface. At any location along the basin interior, and above the deep stagnant fluid, we therefore observe an essentially two-layer system which is locally (over small horizontal distances) similar in configuration to the one-dimensional mixing experiments of, for example, Turner (1968); Deardorff, Willis & Stockton (1980); and Hannoun & List (1988), among others. We therefore envisage the upper layers of our system as a horizontal series of many narrow 'one-dimensional' mixing experiments, each joined laterally. A general result of such experiments is that fluid is *entrained*, or transported, from the lower non-turbulent layer into the upper turbulent layer. In our system, the cumulative effect of this is a recirculation of fluid between the upper layers in the basin.

In order to investigate the recirculation process quantitatively, we consider the turbulent Richardson number, defined as

$$R_j = \frac{\Delta b h}{\sigma_u^2}, \tag{4.1}$$

where Δb is the buoyancy difference between layers, h is the integral lengthscale of the turbulence, here taken as the scale of the upper-layer thickness (also the sill depth), and σ_u is the r.m.s turbulent horizontal velocity in the well-stirred upper layer. In previous 'one-sided' (turbulence on only one side of the density interface) experiments, results have generally shown that the normalized entrainment velocity scales with R_j according to

$$\frac{u_e}{\sigma_u} \sim R_j^{-n}, \tag{4.2}$$

which is valid in the range $1 \lesssim R_j \lesssim 100$ (Hannoun & List 1988). In our case the entrainment velocity u_e may be interpreted as the average volume flux, per unit area, across the interface from the middle layer to the upper layer. A brief summary of one-dimensional mixing experiments is given by Fernando & Hunt (1999) who described details of various entrainment mechanisms. They noted that several independent and methodically varied studies have shown $1.2 < n < 1.75$. In using (4.2) to provide a first-order estimate for entrainment in our experiments, we shall take $n = \frac{3}{2}$, which was shown to give close agreement between (4.2) and the experiments of Turner (1968) and Hannoun & List (1988). Most one-dimensional mixing experiments are conducted in the absence of shear and, while our experiments do include shear, estimates (not presented here) indicate that turbulence in the vicinity of the interface is completely dominated by convection.

Consistent with our results in § 3, we have

$$\sigma_u^2 = \overline{u'u'} \sim \frac{B_o^{2/3} h}{x_v^{1/3}}, \tag{4.3}$$

and

$$\Delta b \sim \frac{(B x_v)^{2/3}}{h}. \tag{4.4}$$

Combining (4.1), (4.3) and (4.4) we find,

$$R_j \sim \frac{x_v}{h}, \tag{4.5}$$

i.e. a linear variation of R_j along the basin. Measurements of σ_u obtained from DPTV results, along with individual buoyancy profiles at the three thermistor locations (t_2,

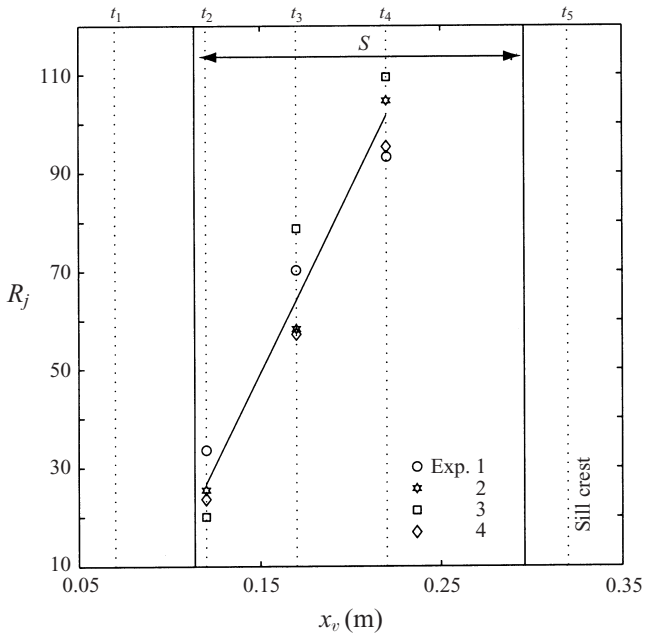

FIGURE 8. The variation of R_j along the basin for experiments 1–4 (symbols). A solid line, representing a least-squares fit to the measured data, indicates the linear scaling of equation (4.5). Thermistors are labelled along the top.

t_3, and t_4) within S (see figure 6*b*), were used to calculate R_j and the variation, for experiments 1–4, is shown in figure 8. While we have only a few points, the solid line fitted to the data supports the linear variation predicted by the simple result in (4.5). The equation for the solid line in figure 8 suggests a best fit $R_j \approx 19(x_v/h) - 63$ for the experiments.

A scaling relationship for u_e may be obtained by combining (4.2), (4.3) and (4.5) which leads to

$$u_e \sim \frac{B_o^{1/3} h^2}{x_v^{5/3}}. \tag{4.6}$$

By definition, the vertical buoyancy flux due to entrainment is $B_e = \Delta b u_e$ or, from (4.4) and (4.6),

$$B_e = C\left(\frac{B_o h}{x_v}\right), \tag{4.7}$$

and C is a constant of order 1. The horizontal transport of buoyancy in the upper layer,

$$Q_b = \int_{z_o}^{H} ub \, \mathrm{d}z, \tag{4.8}$$

varies horizontally, due to both the surface flux and entrainment, according to

$$\frac{\partial Q_b}{\partial x} = B_o + B_e. \tag{4.9}$$

The change ΔQ_b between two horizontal locations (x_a and x_b) is obtained by inte-

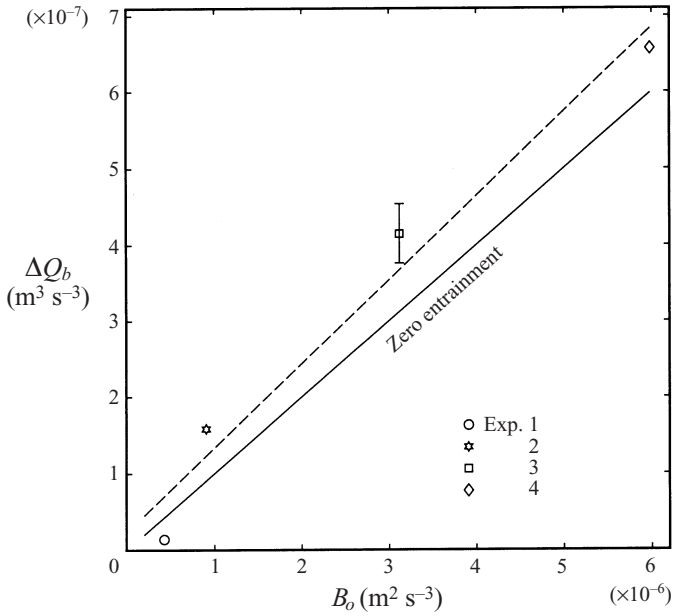

FIGURE 9. ΔQ_b between thermistors t_2 and t_4 as a function of the surface buoyancy flux B_o. The solid line, with slope Δx, represents the expected variation in the absence of entrainment. The dashed line, representing a least-squares linear fit to the measured data (symbols), indicates the actual ΔQ_b which includes the contribution from the entrainment flux B_e.

grating (4.9),

$$\Delta Q_b = \int_{x_a}^{x_b} \left(B_o + C\frac{B_o h}{x_v} \right) \mathrm{d}x_v = B_o \left\{ \Delta x + Ch \ln\left(\frac{x_b}{x_a} \right) \right\}, \tag{4.10}$$

where $\Delta x = x_b - x_a$.

If the Richardson number is very large throughout the domain then there is effectively zero entrainment and from (4.10), $\Delta Q_b = B_o \Delta x$, as shown in figure 9 as a solid straight line with slope Δx. By combining and integrating measured profiles of u and b according to (4.8), we evaluated ΔQ_b between thermistors t_2 and t_4, for each experiment, and the results are shown as symbols in figure 9. The reader is reminded that, although values from only four measurement locations are shown, each of these represent the temporal average of $O(10^3)$ individual measurements. From (4.10) the slope of a line though the measured data should be $\Delta x + Ch \ln(x_4/x_2)$. A least-squares linear fit to the data (shown as a dashed line in figure 9) provides an estimate for the constant $C = 0.9$. Equation (4.7) therefore suggests $B_e \approx 0.9(B_o h)/x_v$. Approximately mid-way along the basin ($x_v = 0.06 + 0.25/2 \approx 0.2$ m) the entrainment buoyancy flux $B_e \approx 0.1 B_o$, or 10% of the surface flux. While this is relatively small, it does have an affect on the final buoyancy of the outflow at the sill and therefore on the value of q_*.

4.2. *Sill–basin equilibrium*

As discussed in § 1, at steady state the exchange rate q across the sill is given by (1.4) but related to the density contrast by the requirement (1.3), i.e. $qg' = B_o L$. The maximal exchange condition was stated in equation (1.5) and the proximity of submaximal flows to this theoretical limit is given by the relative volumetric exchange q_*, defined in (1.6).

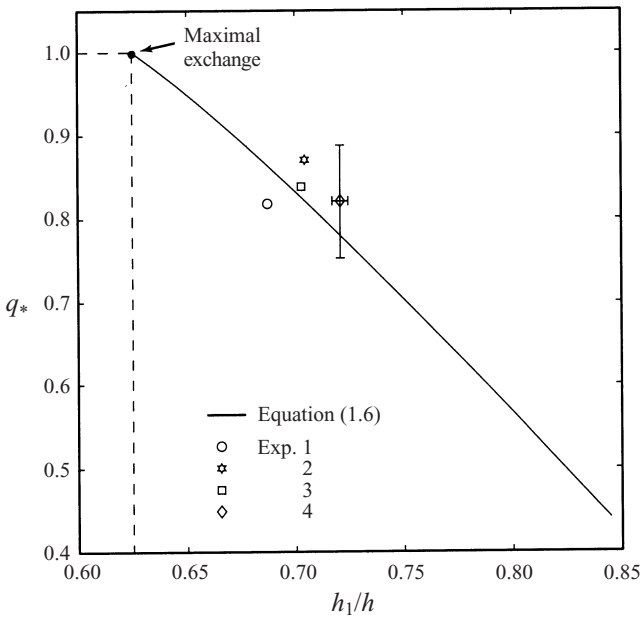

FIGURE 10. The relationship between q_* and h_1/h at the sill crest. A solid curve, representing equation (1.6), depicts the relationship over the submaximal range ($1 > q_* > 0$, $0.625 < h_1/h < 1$). Measured experimental values are shown as symbols.

The buoyancy scaling $g' \sim (B_o L)^{2/3}/h$ suggests that g' at the sill should increase with B_o. This scaling argument lacks the influence of the variable layer depth at the sill h_1 and should therefore be tested. Measured values listed in table 1 confirm the positive correlation between B_o and g'. The only anomalous value is that of g' for experiment 2 which is slightly lower than that for experiment 1, for reasons unknown. Despite this, it appears that the absolute response of q and g' is somewhat predictable; however it is not clear *a priori* whether the relative exchange at the sill moves towards or away from the maximal limit, or if it remains constant. Equation (1.6) suggests that q_* does not depend on the forcing B_o. However, we must examine the relationship between q_* and h_1 to determine if this is entirely true.

The interior processes and sill control are inter-dependent and, when steady, the system is therefore in equilibrium. By changing B_o and allowing the system to reach equilibrium, we were able to observe any changes in the values of h_1 and q_*. The solid curve plotted in figure 10 represents equation (1.6) and it defines the submaximal range. The theoretical maximal exchange limit occurs where $q_* = 1$ and $h_1/h = 0.625$. The reader is reminded that this condition follows from an assumption of infinitely deep reservoirs and the maximal exchange value of q_* in the experiments may actually be slightly greater than unity. Results derived from mean flow measurements of q and h_1 for experiments 1–4, between which only B_o varies, are shown as symbols in figure 10.

At first glance, there appears to be little variation between the experiments. One is led to the conclusion that q_* is essentially constant with a value of approximately 0.85. However, we note that the measurement of h_1/h is significantly more accurate than that of q_* and any variation between experiments should therefore be sought along the abscissa in figure 10. If a vertical line were extended from each data point to the theoretical curve, then the intersections would mark out a consistent rightward shift

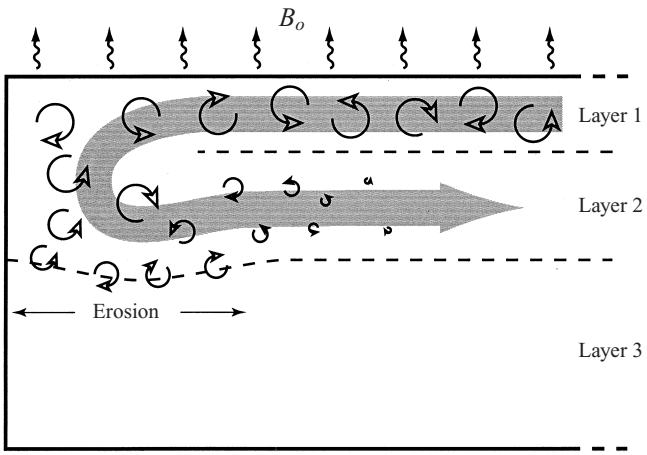

FIGURE 11. Schematic of the dynamics in the vicinity of the basin endwall. The size of the circular arrows implies the relative strength of the turbulence.

along the curve with increasing B_o. The only anomalous point is again experiment 2 (although it is within error bounds of being in the expected order). We therefore conclude that q_* is approximately constant but subject to slight variations due to changes in h_1.

5. Long-term erosion of stagnant fluid

In addition to the issues dealt with in the preceding sections we wish to highlight the potential for the circulating layers (1 and 2) to also slowly erode fluid from the underlying stagnant layer 3 through the process of turbulent entrainment. Earlier we introduced visual evidence of this behaviour in figure 2. It was observed that fluid was eroded more rapidly with increasing B_o. Upon closer inspection it appears that most of the entrainment occurs near the basin endwall where fluid from layer 1, with energetic convective turbulence, is advected down and directly impinges upon layer 3, as shown schematically in figure 11. The turbulence subsequently decays through dissipation and conversion to potential energy, as qualitatively apparent in figure 2 and as shown quantitatively above in § 3.3.

Again, we utilize the scaling suggested by previous one-dimensional mixing experiments (e.g. Hannoun & List 1988) and assume that (4.2) is locally valid in the vicinity of the interface between layers 2 and 3. Basin-scale estimates of σ_u and the buoyancy difference between layers 2 and 3, Δb_{23}, are obtained from (4.3) and (4.4) by substituting the length of the basin L for the horizontal coordinate x and by introducing l as the average integral lengthscale of the turbulence in layer 2. The average entrainment velocity is thus

$$u_{e_a} \sim \frac{B_o^{1/3} l^2}{L^{5/3}}, \tag{5.1}$$

which is simply a generalization of (4.6), where an upper bound on the scale l may be taken as the average thickness of layer 2.

While our measurements from experiments 1–4 are not of sufficient resolution to accurately assess the spatial and temporal variation of u_e we may use experiments 5–8 to estimate the average value. Referring back to figure 2 we again note that, as

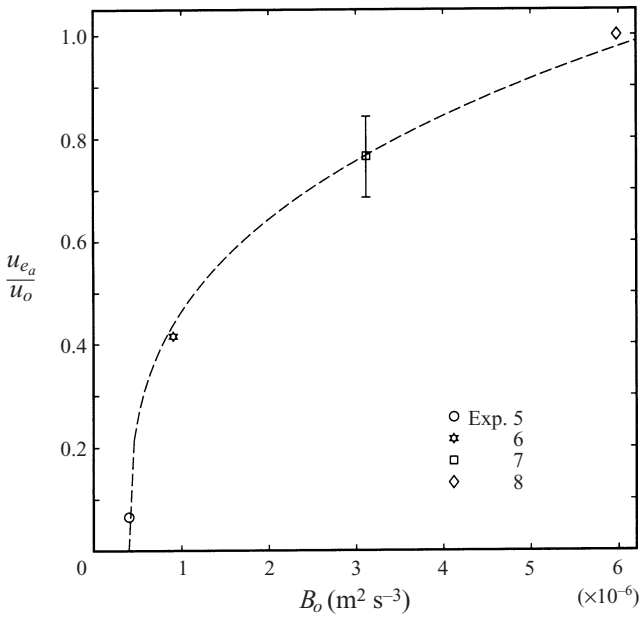

FIGURE 12. Variation of the average entrainment velocity u_{e_a} at the interface between layers 2 and 3, normalized by the maximum measured value u_o, for experiments 5–8. The $B_o^{1/3}$ scaling predicted by equation (5.1) is shown as a dashed line.

B_o is increased, the volume of fluid V that has been eroded from layer 3 at the time T of the photograph also increases. The measured basin-scale average entrainment velocity associated with the erosion of layer 3 is given by

$$u_{e_a} = \frac{1}{WL}\frac{V}{T}, \tag{5.2}$$

where W and L are the width and length of the basin respectively. This quantity was measured from the photographs of experiments 5–8 and the measured values are shown as symbols in figure 12. The $B_o^{1/3}$ scaling associated with (5.1) is shown as a dashed line, where we have assumed l is approximately constant. Despite the crudity of the averaging procedure the measurements show a remarkable adherence to the predicted trend. If we assume that $l \sim h$ then the result shown in figure 12 implies $u_{e_a} \approx 4(h^2/L^{5/3})B_o^{1/3}$ although the h and L dependence has not been tested here. The intersection of the curve with the abscissa suggests that entrainment virtually ceases for $B_o \lesssim 5 \times 10^{-7}\,\mathrm{m^2\,s^{-3}}$.

6. Summary and discussion

Hydraulically controlled exchange over the sill at the mouth of a convectively driven basin is dynamically linked with processes in the basin interior. This link requires the two components of the system to be at equilibrium when the flow is steady and the process by which this state is achieved may be thought of as follows. Turbulent convection due to the destabilizing effect of the surface buoyancy flux sustains a mixed region in the inflowing upper layer. A horizontal buoyancy gradient (increasing in the positive x direction) exists within this region. As we have demonstrated, the effects of this gradient are approximately balanced by inertia, Reynolds stress and surface

pressure. The balance establishes the approximate location of the exchange rate within the available submaximal range. The magnitude of the friction term reported in § 3.3 comes directly from measurements of Reynolds stress. There may also be a contribution from viscous drag at the upper and lower bounds of layer 1 but this has been assumed small compared to the turbulent stress. In very weakly forced flows this assumption becomes invalid.

Recirculation within the basin affects the density at the outflow and thus influences the internal hydraulic control at the sill. As the control condition involves both layers of the exchange, some of the influence of the recirculation is fed back into the basin through the upper layer. When the system is at steady state the exchange q is largely determined by the large-scale momentum balance. The exchange relative to the maximal limit is however a result of the equilibrium between interior processes and hydraulic control.

This study was performed in an effort to highlight the coupled dynamics of the system. As entrainment and recirculation are essential to the process we used a short basin which limited the vertical stratification while allowing significant levels of turbulence intensity to be produced in the upper layer. The results indicated that the buoyancy flux between the upper and middle layers may be up to 10% of the surface forcing flux. An increase in friction or recirculation within the basin will shift the exchange in the direction away from the maximal limit. Both recirculation and friction appear to increase with B_o, leading to a decrease in the relative exchange q_*.

It is quite likely that in long basins there would be very little recirculation owing to large values of R_j along a significant portion of the basin. Our experiments showed that $R_j \sim x_v/h$ and that values of $R_j \sim 100$ were attained within the length of the basin (for which $L = 0.25\,\mathrm{m}$ and $h = 0.025\,\mathrm{m}$). Previous mixing experiments (e.g. Hannoun & List 1988) have shown that turbulent entrainment ceases for $R_j \gtrsim 100$, beyond which transport occurs by molecular diffusion only. In our basin $x_v/h \sim L/h = 10$ and, together with the above results, this suggests that turbulent entrainment diminishes greatly or disappears for values of x greater than about $10h$; however, more work is needed to determine this cut-off value precisely. Recent experiments, conducted by Grimm & Maxworthy (1999) in a relatively long basin ($L = 2.5\,\mathrm{m}$ and $h = 0.05\,\mathrm{m}$), showed that mixing was absent for $x \gtrsim H$ from the basin endwall (where $H = 0.1\,\mathrm{m}$ for their experiments). In this case, our above argument predicts that entrainment occurs only for $x \lesssim 0.5\,\mathrm{m}$ which seems consistent with their observations. Such *long* basins ($L/h \gg 10$) therefore represent a different class of systems within which different scaling laws must prevail. As shown by Grimm & Maxworthy (1999), the scaling of Maxworthy (1997) seems appropriate along most of the long basin. Interestingly, in figure 7 of Grimm & Maxworthy (1999) there appears to be a slight change in the slope of the scaled g' (or b in our case) data within a relatively short region close to the endwall ($-0.2 < \log(x/L) < 0$). The actual scaling in this region could correspond to that observed in our short basin. Owing to the absence of entrainment, variations of the relative exchange q_* in long basins, due to changes in B_o, would be dominated by the effects of friction.

In addition to the dynamics of the upper layers we investigated the process of ventilation or removal of stagnant deep water. Basin-averaged estimates of the entrainment rate of deep water into the middle outflowing layer were made from visual measurements in four experiments across which B_o was varied. These estimates were found to agree closely with a scaling relationship based on a $B_o^{1/3}$ dependence. The results of § 5 suggest ventilation timescales for geophysical systems. For example, in a typical lake or reservoir sidearm one might find $h \sim 5\,\mathrm{m}$, $L \sim 1500\,\mathrm{m}$, $H \sim 15\,\mathrm{m}$, $W \sim 200\,\mathrm{m}$,

and $B_o \sim 10^{-7}\,\mathrm{m^2\,s^{-3}}$ giving $\Delta b_{23} \sim 0.001\,\mathrm{m\,s^{-2}}$. If these forcing conditions were maintained then our results imply $u_{e_a} \approx 2 \times 10^{-6}\,\mathrm{m\,s^{-1}}$ and therefore the deep water would be completely removed from the basin on a timescale $T \sim (H - h)/u_{e_a} \sim 50$ days. While this seems quite short, conditions are never constant for this period of time, and such purging of a sill-enclosed lake sidearm is unlikely. Nevertheless, the results demonstrate that surface cooling can have a significant influence on the residence time of deep basin water. Substantial volumes may even be removed on diurnal timescales in strongly forced shallow systems.

In contrast, we consider the deep water in the Red Sea. This water is replenished by excessively dense water which originates in the Gulf of Suez and drains down the continental slope at the northern end of the sea (Woelk & Quadfasel 1996; Maxworthy 1997). In winter, the volume flux from the Gulf of Suez has been estimated at 0.12–$1.17 \times 10^6\,\mathrm{m^3\,s^{-1}}$ (Woelk & Quadfasel 1996). Considering the lengthscales of the Red Sea with $B_o \approx 4.4 \times 10^{-8}\,\mathrm{m^2\,s^{-3}}$ (Phillips 1966) we estimate the entrainment flux of bottom-layer fluid into the outflowing layer, due to the mechanism described in § 5, to be several orders of magnitude less than the inflow from the Gulf of Suez. It is indeed negligible. Therefore the excess deep water in the Red Sea must exit over the sill at the strait of Bab al Mandab by some other means. In conclusion, it appears that long basins, with relatively weak convective forcing, do not experience flushing of deep water by the entrainment mechanism described above.

The research was supported by the Australian Research Council and an OPRS scholarship to the first author. Our gratitude is extended to Andy Hogg, Jeff Sturman and Kraig Winters who commented on an earlier version of the manuscript. We also thank Chris Garrett for many constructive comments.

REFERENCES

Anis, A. & Moum, J. N. 1994 Prescriptions for heat flux and entrainment rates in the upper ocean during convection. *J. Phys. Oceanogr.* **24**, 2142–2155.

Armi, L. 1986 The hydraulics of two flowing layers with different densities. *J. Fluid Mech.* **163**, 27–58.

Armi, L. & Farmer, D. M. 1987 A generalization of the concept of maximal exchange in a strait. *J. Geophys. Res.* **92**, 14679–14680.

Armi, L. & Farmer, D. M. 1988 The flow of Mediterranean water through the Strait of Gibraltar. *Prog. in Oceanogr.* **21**, 1–105.

Bray, N. A., Ochoa, J. & Kinder, T. H. 1995 The role of the interface in exchange through the Strait of Gibraltar. *J. Geophys. Res.* **100**, 10755–10776.

Cowen, E. A. & Monismith, S. G. 1997 A hybrid digital particle tracking velocimetry technique. *Exps. Fluids.* **22**, 199–211.

Deardorff, J. W., Willis, G. E. & Stockton, B. H. 1980 Laboratory studies of the entrainment zone of a convectively mixed layer. *J. Fluid Mech.* **100**, 41–64.

Farmer, D. M. & Armi, L. 1986 Maximal two-layer exchange over a sill and through the combination of a sill and contraction with barotropic flow. *J. Fluid Mech.* **164**, 53–76.

Fernando, H. J. S. & Hunt, J. C. R. 1997 Turbulence, waves and mixing at shear-free density interfaces. Part 1. A theoretical model. *J. Fluid Mech.* **347**, 197–234.

Finnigan, T. D. & Ivey, G. N. 1999 Submaximal exchange between a convectively forced basin and a large reservoir. *J. Fluid Mech.* **378**, 357–378.

Garrett, C., Bormans, M. & Thompson, K. 1990 Is the exchange through the Strait of Gibraltar maximal or submaximal? In *The Physical Oceanography of Sea Straits* (ed. L. J. Pratt), pp. 271–294. NATO ASI Series, Kluwer.

Grimm, T. & Maxworthy, T. 1999 Buoyancy-driven mean flow in a long channel with a hydraulically constrained exit condition. *J. Fluid Mech.* **398**, 155–180.

Hannoun, I. A. & List, E. J. 1988 Turbulent mixing at a shear-free density interface. *J. Fluid Mech.* **189**, 211–234.

Maxworthy, T. 1997 A frictionally and hydraulically constrained model of the convectively driven mean flow in partially enclosed seas. *Deep-Sea Res.* **44**, 1339–1354.

Murray, S. P. & Johns, W. 1997 Direct observations of seasonal exchange through the Bab al Mandab Strait. *Geophys. Res. Lett.* **24**, 2557–2560.

Nihoul, J. C. J. (Ed.) 1982 *Hydrodynamics of Semi-enclosed Seas, Proc. 13th Intl Liege Colloq. on Ocean Hydrodynamics.* Elsevier.

Niiler, P. P. & Kraus, E. B. 1977 One-dimensional models of the upper ocean. In *Modelling and Prediction of the Upper Layers of the Ocean* (ed. E. B. Kraus), pp. 143–172. Pergamon.

Phillips, O. M. 1966 On turbulent convection currents and the circulation of the Red Sea. *Deep-Sea Res.* **13**, 1149–1160.

Raffel, M., Willert, C. & Kompenhans, J. 1998 *Particle Image Velocimetry*. Springer.

Shay, T. J. & Gregg, M. C. 1986 Convectively driven turbulent mixing in the upper ocean. *J. Phys. Oceanogr.* **16**, 1777–1798.

Smeed, D. 1997 Seasonal variation of the flow in the strait of Bab al Mandab. *Oceanol. Acta* **20**, 773–781.

Stommel, H. & Farmer, H. G. 1953 Control of salinity in an estuary by a transition. *J. Mar. Res.* **12**, 13–20.

Sturman, J. J. & Ivey, G. N. 1998 Unsteady convective exchange flows in cavities. *J. Fluid Mech.* **368**, 127–153.

Tennekes, H. & Driedonks, A. G. M. 1981 Basic entrainment equations for the atmospheric boundary layer. *Boundary Layer Met.* **20**, 515–531.

Tragou, E. & Garrett, C. 1997 The shallow thermohaline circulation of the Red Sea. *Deep-Sea Res.* **44**, 1355–1376.

Turner, J. S. 1968 The influence of molecular diffusivity on turbulent entrainment across a density interface. *J. Fluid Mech.* **33**, 639–656.

Woelk, S. & Quadfasel, D. 1996 Renewal of deep water in the Red Sea during 1982–1987. *J. Geophys. Res.* **101**, 18155–18165.